Design and characterization of a dead-time regime enhanced early photon projection imaging system

L. Sinha,¹ M. Fogarty,¹ W. Zhou,² A. Giudice³, J. G. Brankov^{1,2} and K. M. Tichauer¹

¹Biomedical Engineering, Illinois Institute of Technology, Chicago, 60616, USA

Abstract

Scattering of visible and near-infrared light in biological tissue reduces spatial resolution for imaging of tissues thicker than 100 microns. In this study, an optical projection imaging system is presented and characterized that exploits the dead-time characteristics typical of photon counting modules based on single photon avalanche diodes (SPAD). With this system, it is possible to attenuate the detection of more scattered late-arriving photons, such that detection of less scattered early-arriving photons can be enhanced with increased light intensity, without being impeded by the maximum count rate of the SPADs. The system has the potential to provide transmittance based anatomical information or fluorescence based functional information (with slight modification in the instrumentation) of biological samples with improved resolution in the mesoscopic domain (0.1-2 cm). The system design, calibration, stability, and performance were evaluated using simulation and experimental phantom studies. The proposed system allows for the detection of very-rare early-photons at a higher frequency and with better signal-to-noise ratio. The experimental results demonstrated over a 3.4-fold improvement in the spatial resolution using early photon detection vs. conventional detection, and a 1000-fold improvement in imaging time using enhanced early detection vs. conventional early photon detection in a 4-mm thick phantom with a tissue-equivalent absorption coefficient of $\mu_a = 0.05 \text{ mm}^{-1}$, and reduced scattering coefficient of μ_s ' = 5 mm⁻¹.

I. INTRODUCTION

Analysis of human tissue biopsy specimens currently requires time-consuming and destructive histology procedures that often fail to provide a complete picture of the three-dimensional organization of the tissue ^{1,2}. This can be particularly problematic for cancer specimens where selective tissue sectioning may not represent the heterogeneity of the disease³, or in the case of lymph node assessment, where microscopic populations of cancer may be missed^{4,5}. As such, there are efforts to develop so-called mesoscopic imaging systems capable of providing high (< 1 mm) resolution in tissues up to about 1 cm in thickness (the typical size of a human lymph node or large biopsy)⁶. Optical projection tomography (OPT) is one of the promising modalities emerging in this field, where the transmission of excitation or fluorescence light—typically in the near-infrared spectral range, 600-1000 nm, where tissue absorption is relatively low⁷—is imaged at multiple projections around an object⁸. However, because the light scattering in tissue limits imaging resolution, most OPT applications require samples to be relatively transparent or optically cleared⁹, and even then, diameters should be no larger than a millimeter or two.

To reduce the negative impact of scattering on image resolution in optical projection imaging, a number of approaches have been developed to either restrict highly scattered photons from reaching the detector (e.g., through time-gated detection of the earliest arriving photons¹⁰⁻¹³, angular restriction¹⁴, harmonic holography¹⁵, or beamshaping¹⁶), to account for scattering in image reconstruction models^{17, 18}, or to employ phase contrast techniques that are less dependent on scattering¹⁹. This work details and evaluates an optical projection imaging system capable of OPT data collection that employs what we term "dead-time enhanced early-photon detection." This allows the capture of very rare early photons, i.e. the ones that have taken the most direct path between the source and detector²⁰, at a higher frequency and with better signal-to-noise ratio compared to other approaches.

A. Time-domain and early photon detection

The high probability of light scattering in tissue (approximately 10 scattering events per mm traveled by a photon)⁷ and the stochastic nature of scattering, mean that every detected photon may take a unique path through the tissue and the length of that path will vary from photon to photon. Time-domain detection systems measure the arrival times of photons from pulsed light sources providing data in the form of a temporal point spread function (TPSF, **Fig 1a**)²¹. While most detected photons undergo multiple scattering events in tissues greater than 1 mm in thickness, a small percentage will take a more direct route through the tissue with minimal scattering (**Fig 1b**). These are the early arriving photons, which, if collected in sufficient numbers, can be used exclusively to reconstruct higher resolution images than the ones reconstructed using mainly later-arriving photons^{11, 12, 22-25}.

²Electrical and Computer Engineering, Illinois Institute of Technology, Chicago, 60616, USA

³MPD Micro-Photon-Devices, via Stradivari 4 – 39100, Bolzano, Italy

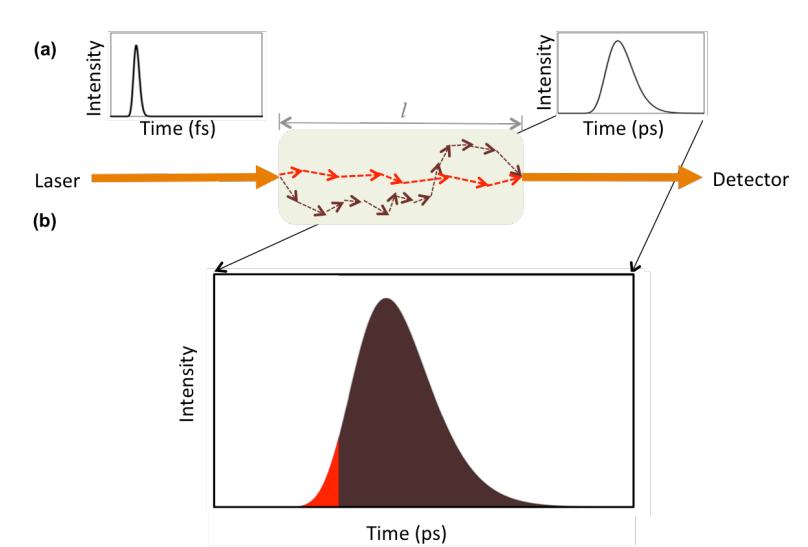


Figure 1. Propagation of photons through a tissue. (a) An illustration depicts how a laser pulse broadens in the time-domain as it travels through a highly scattering medium such as biological tissue; temporal profiles of the light input and output are presented with respect to their normalized intensities. The red arrows indicate the path of a photon might take with minimal scatter, while most photons take a more circuitous path, an example of which is represented by the brown arrows. (b) The corresponding colors in the detected temporal point spread function represent the earlier arrival of the minimally scattered photons.

For applications in diffuse biomedical optical imaging (light detection through scattering biological tissue), a number of approaches have been explored to isolate the early arriving photons. These have included time-gated detectors based on either intensifier^{11,25} or second harmonic generation optical shutters^{10,12,13}, streak cameras²⁶, and time-correlated single photon counting (TCSPC)²⁷⁻²⁹. All methods have demonstrated improved spatial resolution over conventional diffuse optical imaging, achieving resolutions as low as 50 µm through a 2-mm thick tissue²². In general, time-gating approaches allow a higher frequency of early photon detection, as detectors are not overwhelmed by the more abundant later arriving photons and laser intensity can be increased up to tissue safety levels to achieve the desired early photon count rates. The downside to time-gated detection is that the arrival time of the early photons is dependent on sample thickness, which may vary over the volume of the sample, so use of a consistent gate for all data projections may fail to identify early photons at all locations. Streak camera and TCSPC approaches will always capture the earliest photons (since all arrival times are equally sampled); however, the majority of the dynamic range of these detectors will be occupied by the more abundant diffuse photons, therefore restricting the early photon detection rate. Recently, our group proposed a method capable of early-photon collection at high counting rates, without the ambiguity of gate placement, by carrying out TCSPC measurements with SPAD-based photon counting modules and exploiting their unique dead-time characteristics ²⁰.

B. Principles of dead-time enhanced early photon detection

Normally, for acquiring a TPSF, TCSPC is used. With these techniques, it is possible to reconstruct a fast pulse at temporal resolutions not possible with analog avalanche photodiodes (APDs)—owing to bandwidth and/or sensitivity limitations—by using single-photon detectors such as photomultipliers tubes (PMT) or single-photon avalanche diodes (SPAD). The TCSPC method is based on the precise time stamping of the arrival times of each single-photon impinging the detector, measured in respect to a triggering event (typically a synchronization signal generated by the pulsed laser used for the excitation). The counts are accumulated in a histogram that is "built up" by repeated pulsing of the laser and accumulation of single-photon counts until statistically sufficient number of events is acquired. As single photon counters typically do not have photon number resolving capabilities (i.e. the ability to count the number of photons arriving at the same time) and, like any TCSPC time sorter, are blind for a well-defined period following each triggering (dead-time). Typically, light pulse intensities arriving at the detector are attenuated such that the probability of having two or more photons reach the detector per pulse is low. In this way it is possible to obtain a system that measures the probability of detecting a photon at *any* arrival time, instead of the probability of detecting the *first* photon. This is normally obtained by making sure that the detector count rate is lower than 5% (or better, 1%) of the excitation laser repetition rate³⁰.

A TPSF is thus obtained, with the standard TCSPC method, by repeatedly measuring the transit times of photons travelling through the tissue, as the time difference between the light source sync signal and the single-photon detection event. As many photons must be collected and time-stamped from many light pulses³⁰, this technique is very lossy and time-consuming. However, for early photon imaging applications, there is no need to collect the later arriving photons. In fact, in this case, the information is in the early (first) photons to arrive at the detector and not in the late ones that can and should be discarded. If a late photon arrives during the dead-time caused by an earlier photon, neither will it contribute to the count rate of the detector, nor will it produce a dead-

time, which could mask any subsequent early photons from the following pulse. This allows a user to increase the light source intensity to any level to achieve the desired count rate of rare early photons at the expense of the far more abundant and diffuse late-arriving photons²⁰. Indeed, TCSPC 5% (1%) limitation is no longer required. Of course, this dead-time masking is beneficial as long as the detector is not damaged by high photon illumination. We call this new time-domain technique: dead-time enhanced detection of rare early-photons. While the principle of enhancing the detection rate of early photons was demonstrated in a previous article²⁰, this paper provides an indepth description and evaluation of an optical imaging system optimized for incorporation of enhanced early photon imaging. Specifically, it includes an optimization of the lens assembly, measurements of system stability, measurement of the instrument response function, demonstration of enhanced signal to background at high early photon count rates (up to 3 orders-of-magnitude improvement in the presented system), and a correction method for time shifting of temporal pulse spread functions, attributable to time-walk³¹, at high incidence rate.

SYSTEM DESIGN

A. Overview

The enhanced early photon imaging system is illustrated schematically in Fig. 2a and a photograph is presented in Fig. 2b. In this prototype system, a 780-nm 12-mW femtosecond (< 90 fs FWHM) laser with a pulse rate of 10 MHz (Mendocino, Calmar Laser, Palo Alto, CA) was used as a light source. The light emitted from the laser had a divergence of 0.4 mrad and a beam diameter of 1.5 mm. The illumination light was first directed through a laser cleanup 10-nm band-pass filter centered at 785 nm (ZET785/10x, Chroma Technology, Bellow Falls, VT) and then through a motorized filter wheel containing a range of neutral density filters (Thorlabs, Newton, NJ) to control the intensity of illumination at the surface of a sample. The light was then focused down to a sub-50-µm sized spot on the surface of the sample holder using a 75-mm focal length aspheric doublet lens (Thorlabs; see Section IIC). The sample holder consisted of a clear acrylic tank containing acrylic refractive index matching liquid (Cargille Laboratories, Cedar Grove, NJ) that allowed for free movement of a 1-cm diameter cylindrical acrylic tube used as a sample container, with minimal light distortion. This container was mounted onto a motorized stage assembly (Thorlabs) with 3 degrees-of-freedom (lateral, vertical, rotational) to allow for tomographic imaging in future. A pair of 100-mm focal length aspheric doublet lenses (Thorlabs) was positioned opposite to the illumination component of the system (i.e., at the back of the samples holder), to collect light from a 50-µm diameter region on the back of the sample holder and focus it onto a SPAD (50 µm active area diameter PDM, Micro Photon Devices, Italy). The laser driver and SPAD were connected to a time-correlated single photon counting (TCSPC) module (HydraHarp, PicoQuant, Berlin, Germany), which was designed to time stamp every detected photon with respect to the nearest sync signal coming from the laser driver. Our system dead-time was 77ns. The TCSPC module, filter wheel, and motorized stage assembly were all connected to a PC and controlled using in-house software developed in MATLAB (Mathworks, Natick, MA). An in-depth discussion on the selection of each component of the system is described below.

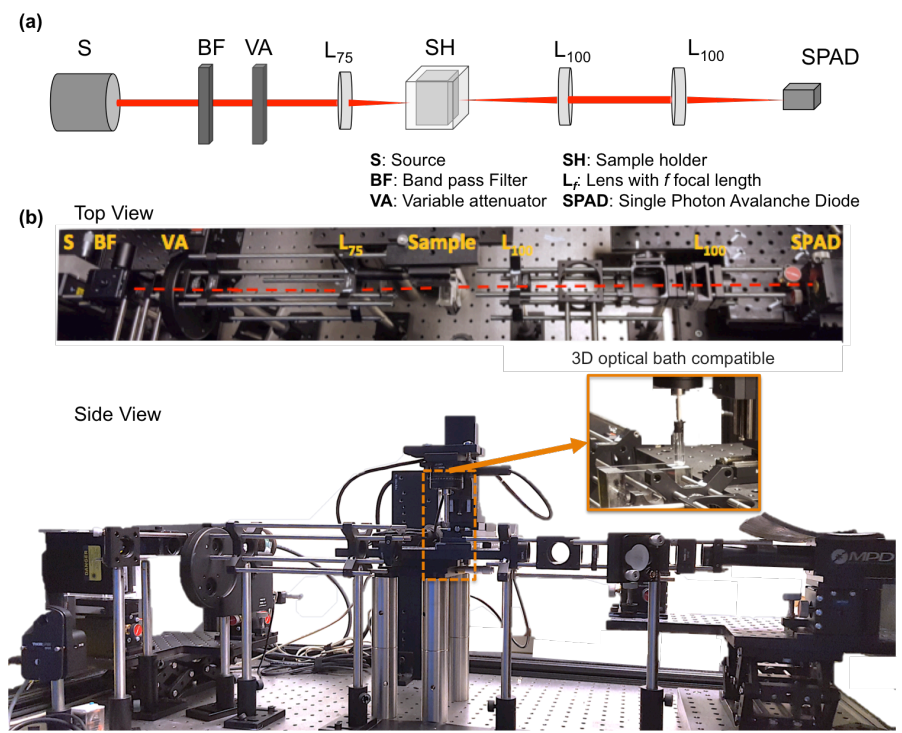


Figure 2. Enhanced early photon projection imaging system. (a) Illustrated schematic of the system.; (b) Top view and side view photograph of the system is presented, with a zoom on the sample holder, which was designed to allow tomographic images of a sample.

B. Laser repetition rate

In order to select the best laser repetition rate for the experiment, detector (SPAD) and TCSPC instrumentation (HydraHarp, PicoQuant), dead-time must be taken into account. As previously discussed, the dead-time for a single photon counter is the time following each avalanche triggering during which the sensor is unable to detect a subsequent photon³², while for a TCSPC instrumentation, it is the time needed by the internal electronics to be able to record another start-stop time difference following a previous measurement. As the HydraHarp and the SPAD have about the same dead-time (77 ns for the PDM, < 80 ns for the HydraHarp), for simplicity, the dead-time was assumed to be attributable only to the detector. It follows that any photon impinging the detector during the deadtime is completely discarded (Fig. 3a). Fig. 3b demonstrates the probability of photon detection as a function of time supposing the ideal detector (100% sensitivity), apart from during the dead-time, and that the laser power is high enough so that many photons per pulse impinge the detector. In this way, the early photons trigger the SPAD immediately as they arrive at the detector thus masking any subsequent photon of the same pulse. As a consequence, the overall photon detection probability quickly decreases in time after the earliest possible photon arrival time (dashed perpendicular line). The higher the number of photons per pulse, the stronger the masking and the faster the decrease in probability of later photon detection. In Fig. 3b, 2.35x10⁹ photons per pulse arriving at the SPAD were simulated. Fig. 3b demonstrates what happens when the laser pulse repetition rate is changed from 10 to 40 MHz, without changing the laser pulse energy. If the laser repetition rate is high enough so that a laser pulse can arrive during a dead time generated by a previous laser pulse, the overall detection efficiency is reduced. For example, by using a laser with a period of 50 ns (20 MHz repetition rate) and assuming a high number of photons per pulse impinging a SPAD with a dead-time of 77 ns, 50% of the laser pulses on average can fall in the dead time of previous pulse thus accordingly reducing the detection probability. Finally, the TPSFs, Q(t), were simulated using a Green's function—denoted G(t)—solution to the diffusion approximation of the radiative transfer equation (assuming an instantaneous source pulse)³³, convolved with an instrument response function, IRF(t):

$$Q(t) = G(t) * IRF(t) = I_o NA \cdot \eta \cdot A \frac{v}{\left(4\pi Dvt\right)^{3/2}} \exp\left(-\frac{l^2}{4Dvt} - \mu_a vt\right) * IRF(t), \tag{1}$$

where, I_0 is the number of photons reaching the surface of the sample in one pulse, NA is the solid angle of light collection at the detector, A is the area of the detector (50-µm diameter, circular), η is the quantum efficiency of the

detector at the wavelength of light employed (0.15), v is the speed of light in the medium, l is the thickness of the tissue, D represents the diffusion coefficient ($D = [3(\mu_a + \mu_s)]^{-1}$), with μ_a and μ_s ' representing the absorption and reduced scattering coefficients, respectively, and the * symbol represents the convolution operator. The IRF(t) was measured directly using the system (see **Fig. 6**). An example of an expected TPSF, in the absence of dead-time effects, is shown in **Fig. 3c** (green dashed curve), with the number of photons corresponding to 6 mW of laser power for 10 MHz laser pulse frequency, and for a tissue of thickness of 4 mm, having optical properties of $\mu_a = 0.02$ mm⁻¹ and μ_s ' = 5 mm⁻¹: typical of biological tissue⁷.

To evaluate the effect of dead-time on high power applications with TCSPC, Q_i was defined as the discrete form of Q(t): specifically, $Q_i = Q(i\Delta t)$, where Δt is the size of the time intervals used to "bin" photon counts by the TCSPC module in creating the numerical TPSF, and $i = 1, 2, 3, ..., (F\Delta t)^{-1}$ —where F is the laser pulse rate. With conventional use of TCSPC (count rates < 5% of the laser pulse rate), the number of photons detected in a given bin (q_i) is identical to Q_i . However, dead-time will reduce the number of detected photons with variability in the reduction effect amongst bins depending on the laser frequency and duration of the dead-time. Similar effects have been modeled previously.³² Here, a modified version of this model is presented that includes the possibility of the dead-time extending over more than one pulse period (dead-time > laser pulse period). The relationship can be defined as:

$$q_i^{k+1} = FQ_i \left[1 - \sum_{j=1-\tau}^{i-1} \frac{q_{\text{mod}(j,M)}^k}{F} \right], \tag{2}$$

where, FQ_i is the number of photons in 1 s of acquisition time, M is the number of time bins between laser pulses (equivalent to the pulse period divided by the time bin) and mod(j, M) performs the modulo operation (generating the remainder when j is divided by M). Each time bin was set to 4 ps to match the time binning of the TCSPC system used in this study, and the dead-time, τ , represented the dead-time in number of time bins (the dead-time of the system used in this study was approximately 77 ns, thus τ was set to 77 ns/4 ps = 19250 bins).

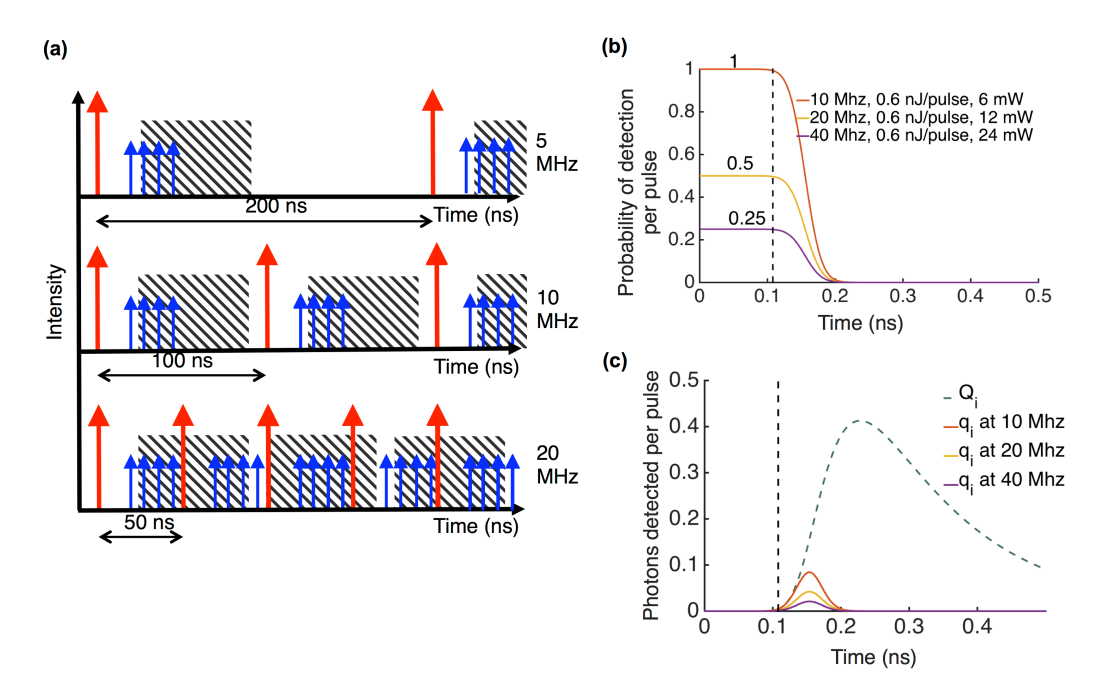


Figure 3. Effects of system dead-time on the probability of photon detection. (a) A schematic depiction of photon rejection when dead-time is triggered for different laser pulse-rates, assuming a dead-time of 77 ns. The red arrow depicts a laser pulse (~90 fs FWHM) while the blue arrows depict arrivals of single photons at the detector. All photons arriving within the dead-time of the detector (striped region), will not be detected. Upon reset, the detector will detect the first subsequent photon.; (b) A simulation study demonstrating a comparison of the probabilities of photon arrival time detection for time-correlated single photon counting procedures of different laser frequencies. Power of light per pulse incident on the detector was maintained for all the frequencies. The probability of detecting photons in each 4 ps bin for a photon arrival rate far exceeding the laser pulse rate for 10, 20, and 40 MHz light sources are shown in orange, yellow, and purple, respectively. The x-axis is arrival time of photons. Note, the range of

the time is arbitrary as it is a difference between arrival time of laser and detector signals. The vertical dashed line represents the arrival time of the first photons coming from the laser. (c) The distribution of arrival of photons detected at the detector during one pulse is presented. The theoretical arrival time distribution of photons per pulse at the detector is shown by the green dashed line, *Qi*. A 4 ps time-binning of photon arrival times was used for the experiment.

The average q_i , q_i^{final} , was calculated by iterating Eq. 2 until the normalized error in q_i^{k+1} between k and $k+1^{th}$ iteration was less than 0.1% relative to value of k^{th} iteration, with initial assumption that $q_i^0 = F \cdot Q_i$. The likelihood of detecting a photon at a particular time bin can then be estimated by:

$$p_i = \frac{q_i^{final}}{Q_i} \ . \tag{3}$$

When the time between photons arriving at the detector was greater than the dead-time, p_i was independent of laser pulse rate, and the earliest arriving photons retained a probability of detection of 1, despite lowered probability of detecting later-arriving photons (left of the black dashed curve in **Fig. 3b** and **3c**). Note: all pulse rates with periods greater than the dead-time of the system will provide identical results to the 10 MHz data presented in **Fig. 3b** and **3c**, and were therefore not shown. This is critical for using early photons for image reconstruction, since measured signal should be proportional to (linear with) the signal intensity reaching the detector. However, for lasers with pulse periods shorter than the dead-time (20, 40 MHz), the probability of early photon detection was reduced, thereby also attenuating detection of early arriving photons in addition to the later photons (bottom of **Fig. 3a**). This would cause increase heat load on tissue being imaged without providing benefit in early photon detection. Therefore 10 MHz was selected as the optimal frequency in the current system to maintain optimal detection efficiency of early photons.

C. Laser focusing lens selection

A 75 mm focal length lens was used to focus the laser beam to a waist (FWHM of width) of less than 50 µm in diameter for a 5 mm wide range at the surface of the sample to ensure limited variability in spot size for small inhomogeneities in the structure of the sample surface, or small system misalignments. This was optimized using a free space Gaussian beam propagation law for each optical element, curved interface, and propagation distance, defined by a transfer matrix (also commonly termed as the ABCD matrix³⁴).

The calculations for various focal length lenses are shown in **Fig. 4a**. One can observe that as long as the focal length of the focusing lens is shorter than 130 mm, the FWHM of the beam, at the focal distance, is smaller than 50 μ m. We also calculated the distance around the focal spot for which the FWHM of the beam was < 50 μ m (assuming the beam traverses through air) for various theoretical focal length lenses as well as for some commercially available lenses (**Fig. 4b**). Here, one can observe that lenses with focal lengths between 50-120 mm satisfy the criterion of producing a spatial range of greater than 5 mm about the focal spot for which the *FWHM*_{beam} is < 50 μ m.

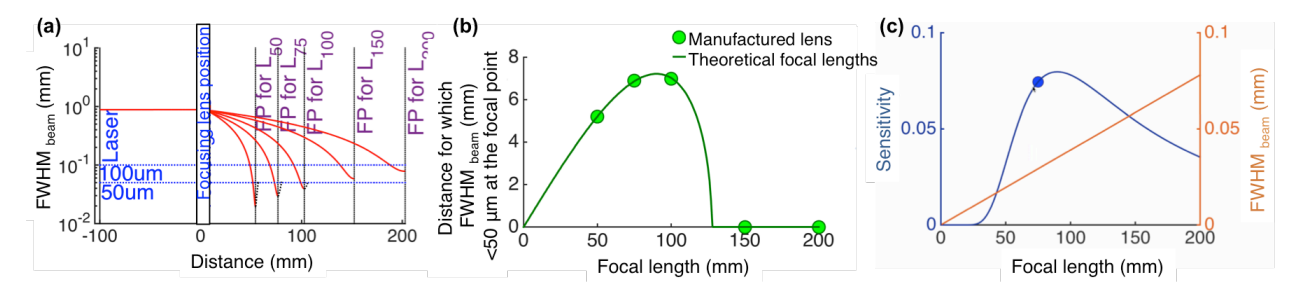


Figure 4. Selection of the laser-focusing lens. (a) The full width at half maximum (FWHM) of the Gaussian beam profile with respect to changing length of focal distance. (b) As the focal length of lens changes the distance for which the FWHM of the beam is below 50 μm varies peaking in the range of 75-100 mm.; (c) The sensitivity at detector is shown with respect to changing focal length of the lens and a highly sensitive lens (75 mm) is used for our purpose with a moderately large FWHM as shown by the blue dot.

To facilitate system alignment and instrument response function measurement a metric for the alignment sensitivity was developed to ensure that the beam waist at the detector, in the absence of an imaging subject, should be such that a slight change in the position of a perfectly centered beam results in a significant change in the measured power at the detector.

Therefore alignment sensitivity was defined as:

$$sensitivity = 1 - \frac{\iint\limits_{Da} g(x - \Delta, y - \Delta; \omega(d_{\text{det}})) dx dy}{\iint\limits_{Da} g(x, y; \omega(d_{\text{det}})) dx dy}, \tag{4}$$

where Δ denotes the displacement of the detector (for example 10 μ m), which is limited by the translation stage on which it was placed, the $g(x,y;\omega(d_{\text{det}}))$ is the Gaussian function representing the beam profile, $\omega(d_{\text{det}})$ represents the beam waist at the detector, and Da is the detector area (50-by-50 μ m). The sensitivity study showed that the lenses between 50 mm and 130 mm provide the highest *sensitivity* (see **Fig. 4c**).

Here we finally selected a 75 mm focal length lens as optimal however a 100 mm lens would be an equally good choice. At full power, the current system focuses a 6 mW beam down to a 50 µm spot size at the surface of the sample, yielding 0.03 mJ cm⁻² per pulse, about 3 orders-of-magnitude below the ANSI safety limit for skin for a single pulsed near-infrared laser 30 mJ cm⁻². Repeated pulsing used in the described system could amplify effects; however, it should be noted that a similar setup with 9 orders-of-magnitude higher light power density demonstrated no change on cellular reproduction of exposed living hamster embryos over 24 h of exposure³⁵.

D. Optical elements before the detector

A bi-telecentric lens design was chosen such that the area of the detector (Section IIE) would match the area of light detection on the surface of the sample. This can be done with any two equal-focal length lenses that are arranged such that the distance between them is double the focal length, the location of the back surface of the sample is positioned at the focal length of the first lens, and the position of the detector is placed at the focal length of the second lens (Fig. 5a). In this work, two 100-mm focal length lenses were selected, as this allowed some constriction of photon acceptance angle (longer focal length lenses have smaller numerical aperture, which can also improve rejection of scattered photons¹⁴), without making the system overly large. Further improvements in detection optics and the trade-off between photon collection rate and angular constriction of detected photons will be investigated in future work.

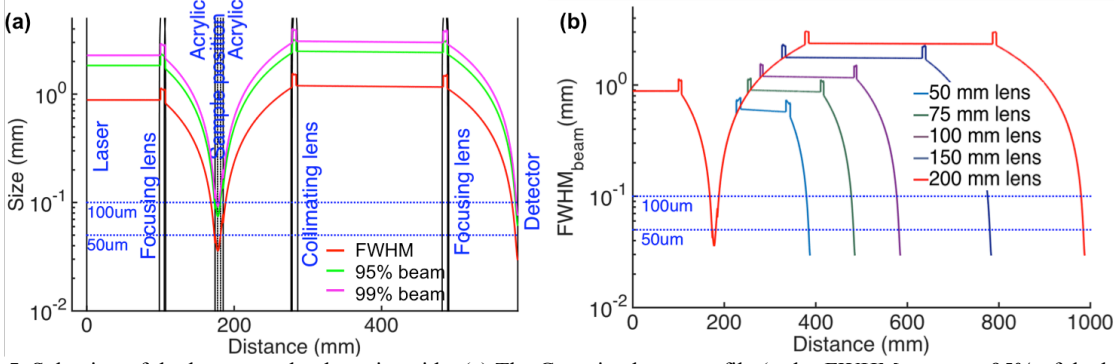


Figure 5. Selection of the lenses on the detection side. (a) The Gaussian beam profile (red = FWHM, green = 95% of the beam; magenta = 99% of the beam) is shown as it passes through different elements in its path (assuming no diffusive medium is placed at the sample position). (b) The same Gaussian profile as shown in (a) varies depending on the focal length of the lenses used at the detection side as observed in—shown here in FWHM.

E. Detector and TCSPC module

Single photon avalanche photodiodes (SPADs) and photomultiplier tubes (PMTs) are two commonly used detectors for single photon detection, a detection scheme that is necessary for time-correlated single photon counting (TCSPC) in time-domain optical systems. A SPAD (PDM Series, Micro Photon Devices, Bolzano, Italy) was selected as the detector in the current system for a two reasons: 1) SPADs typically have much better temporal resolution (lower jitter) compared to conventional PMTs³⁶; 2) SPADs are much more robust than PMTs and can be exposed to high incident light power without damage²⁸.

PDM modules generate electrical output pulses, according to the NIM standard, with 20 ns pulse-width. Their falling edge very precisely marks photon arrival times and thus was fed to the TCSPC module (HydraHarp, PicoQuant) in order to measure the arrival time of each detected photon with respect to the laser pulse. A system instrument response function (IRF), i.e. the convolution of the detector's and the TCSPC instrumentation's IRFs with the laser pulse shape, was determined experimentally to have a FWHM of ~35 ps (Fig. 6a). The SPAD used in

this research also had a dead-time of approximately 77 ns, immediately following each detected photon, which was "non-extendable": any incident photon onto the detector during the dead-time, does not extend the duration of the dead-time. This characteristic is critical for the method of enhanced early photon detection used in the described system (Section IB). The TCSPC module can be run in either time tagging-mode, where the time stamp of each photon with respect to the corresponding laser pulse and the clock time is recorded independently for each event, or in a histogram mode, where photons are binned into desired number of bins (smallest being 1 ps) for a desired length of time. For example 200 ms exposure would include photon detection from 2 million laser pulses using a 10 MHz laser all binned into a single histogram of arrival times. In this study, the TCSPC module was run in histogram mode.

F. System control and data acquisition.

In-house software written in MATLAB 2015a (Mathworks, Natick, MA) installed on a single CPU (Inspiron 3847 with 4th generation Intel® CoreTM i5-4460 processor) was used to control the system. The software controlled all shutters, stages, and the TCSPC module for data acquisition. Specifically, the motorized stages and laser shutter were controlled through ActiveX Controls (Thorlabs) incorporated into the MATLAB environment and the TCSPC module was controlled using MATLAB functions provided by the manufacturer (PicoQuant) in their HHlib library.

A typical experiment requires system stabilization, which is obtained by powering on the system at least 25 minutes before any measurement (Section IIID). After stabilization, the instrument response function (IRF) of the system is measured (Section IIIA), followed by the positioning of the sample in the sample holder. The user is then able to define the area and the spatial pattern for projection data collection, the acquisition duration for each projection, and the laser intensity. All data is then acquired automatically. During the data collection, the motion stages are moving continually and the data collection, at each pixel, is synchronized with stage movement. Each acquired TPSF histogram is saved to a computer hard-drive. The in-house program allows visualization of the acquired data in a form of an image where the display is updated after each line-scan is performed. This helps the users to ensure positioning of the sample remains rigid throughout the scan. After the full acquisition is complete the shutter automatically shuts the laser light off using the laser's interlock system.

II. SYSTEM CHARACTERIZATION

A. Instrument response function (IRF) of system.

The IRF of the system was defined as the measured TPSF of the laser; i.e., the TPSF measured by the system without any sample in the holder (Fig. 2). To avoid potential laser shape differences at different laser operating powers, all measurements in this study were made with the laser running at 95% of full power, while adjusting tunable neutral density (ND) filters, in front of the laser, to control the power incident on the sample. Using this approach for controlling laser power, the IRF of the system was measured over 4 orders-of-magnitude, with the lowest power at a level such that the detector's counting rate was just below the 5% of pulse rate, as required by the TCPSC technique. In all cases, the laser repetition rate was at 10 MHz and the acquisition time was set to 200 ms. The estimated power of the laser hitting the detector in each case was 3.2 μW, 7.6 μW, 69.7 μW, 799 μW, and 8.4 mW, respectively. The full measured IRF of the lowest laser power is presented in Fig. 6a. There was a significant time shift in the IRFs toward earlier time bins for the higher laser power conditions (Fig. 6b). This shift was in accordance with the fact that at high counting rates there is both a statistical distortion of the IRF due to the higher probability in detecting earlier photons respect to the late ones (as described above), but also with a typical effect related to the SPAD's internal physical mechanism exploited to detect single photons. The latter, typically observed in satellite tracking experiments, is referred to as "time walk" Indeed, the time delay between photon absorption and the avalanche current build-up (considering a fixed threshold) depends on the number of incident photons: as more photons are absorbed, the faster the avalanche build-up is and the shorter the time delay (time walk delay). As demonstrated in the subsequent section, the shift can be empirically accounted for, and can also be accounted for in future using hardware advances³¹. The shift was quantified by fitting a 3rd order polynomial to the rising edge of the normalized IRFs and finding the histogram time associated with a count of 5 photons. The shifts were 0 ps, -7 ps, -25 ps, -44 ps, and -90 ps, respectively, compared to the lowest laser power IRF.

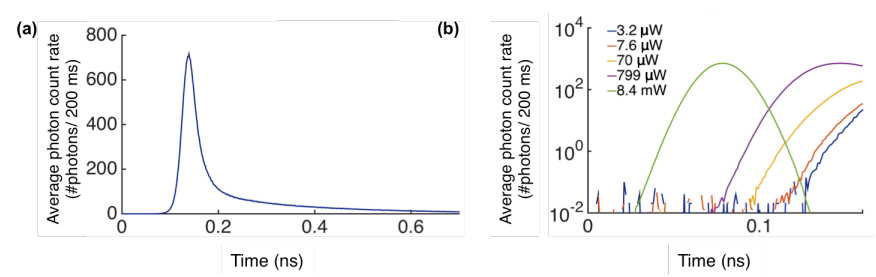


Fig 6. Instrument response function (IRF) of the system. (a) The IRF when the detector is not saturated. FWHM of the IRF is 35 ps. 1 ps time binning resolution of HydraHarp was used for the experiment. (b) The time shift ("time walk") observed in the IRFs with increasing laser power

B. Linearity of early photon signal as a function of laser power.

In order to test the linearity of early photon detection rates at high laser powers—i.e. with detector counting rates much higher than 5% of the laser repetition rate—equivalent light energy scenarios were compared: (1) one with the system at high laser power (e.g., 10 mW) and short exposure time (e.g., 200 ms, for a total light energy delivered at the sample surface of 2 mJ), and (2) one at low laser power (e.g., 0.01 mW so that standard TCSPC conditions were met) and long exposure time (e.g., 200 s, also for the total energy of 2 mJ). Henceforth similar comparisons will be referred to as energy-matched saturation and conventional modes, respectively. Experimentally, a 2-mm-thick 1.7 cm x 2 cm rectangular tissue-mimicking optical phantom (see Section IIIE for details) having absorption and reduced scattering coefficients of 0.05 mm⁻¹ and 5 mm⁻¹, respectively, was placed in the system at the location of the sample holder (Fig. 2a) and a 70/30 beam-splitter (BS) was placed after the first lens on the detection side to split the transmitted beam onto 2 separate SPAD detectors connected to the TCSPC unit. The first detector, accepting 70% of the light, was used to measure the TPSF of the transmitted light; while light from the 30% beam was attenuated with characterized ND filters such that the count rate never exceeded the 5% TCSPC typical limit. The total photon counts, corrected for the absorption of the ND filter and beam splitter, in the second detector were used to estimate the energy of light deposited on the first detector by the following relationship (note: total photon counts on the first detector cannot be used to correctly measure the incident light power due to dead-time effects in case of high photon fluxes):

$$E = N \frac{hc}{\lambda} \frac{1}{ND \cdot 0.70},\tag{5}$$

where 0.7 and ND are the beamsplitter and neutral density filter attenuation, N is the number of photons detected, h is Planck's constant, c is the speed of light, and λ is the wavelength of light used. From an initial detector's incident laser power of 0.01 mW, either (1) acquisition time was varied over 4 orders-of-magnitude (0.2 s, 2 s, 20 s, 200 s) with 0.01mW laser power (conventional mode); or (2). laser power was adjusted with tunable neutral density filters over 4 orders-of-magnitude higher (0.01, 0.1, 1, and 10 mW) with 0.2 s acquisition time (saturated mode).

As expected, at higher laser powers, significant shifts in TPSFs in the saturated mode data were observed with higher energy incidence at the detector tending to shift the TPSFs to earlier time bins (**Fig. 7a**, solid data). To correct for these shifts, the timing of each TPSF was referenced to a power-at-detector matched IRF (**Fig. 7a**, dashed data). More specifically, the TPSFs were simply shifted forward in time by the magnitude of the time difference between the power-matched IRF and the IRF in conventional mode, described in **Section IIIA** (**Fig. 7b**). The number of early photons detected for each energy level was calculated within a given time window defined by 40 bins preceding the time at which the conventional IRF reached 0.7% of the max count rate on the rising slope (**Fig. 7a**, vertical dashed lines). Without correcting for the TPSF time-shifts at higher laser powers, the number of early photons will be grossly overestimated because the TPSF shifted so far as to position the window onto the falling edge of the TPSF (see **Fig. 7 a and d**). In contrast using TPSF time-shifts correction the number of early photons calculated at the highest power is in line with the power-scaled number of photons measured in conventional approach. Finally by employing the time-shift correction described before calculating the number of early photons in the saturation mode TPSFs (**Fig. 7c** displays an example shifted saturation mode TPSF with energy-matched conventional mode TPSFs was observed (**Fig. 7d**; r = 0.99, p < 0.01).

C. Afterpulsing in saturated and conventional modes

Afterpulsing is a phenomenon of many single photon counting detectors (PMT, SPAD). In the case of SPAD detectors it is attributable to the fact that, during an avalanche current pulse, some avalanche carriers can be trapped inside the junction at deep levels and subsequently released with a statistical delay that normally follows an exponential distribution. If these trapped carriers are released after the end of the SPAD's dead-time, they can trigger an avalanche that is correlated with the previous one: the afterpulse. For the SPADs used in the presented system, the decay time-constants of trapped charges, are in the range of microseconds and thus this phenomenon is slow compared to the dynamics of the TPSF³⁷. Furthermore, with a laser repetition rate of 10 MHz, TCSPC acquisitions are repeated every 100 ns and the afterpulsing decay curve, which would start immediately after the end of the dead time, is thus acquired folded many times over the 100 ns observation window. As a consequence, considering the 77 ns dead-time, the 100 ns observation window and the typical experimental start-stop difference, afterpulsing can be very well approximated as a bias offset in the measured TPSFs with a very small peak far away from the TPSF. It follows that the mean of such folding can be subtracted from the data by calculating the "background" signal in a region of the TPSF where no laser pulse is expected to exist. Note, background can be a mixture of dark counting rate (DCR) and afterpulsing; however, dark counts were so rare that the background signal in our experiments were dominated by afterpulsing. The region for background subtraction should be selected close to the initiating of the detected TPSF incase the afterpulsing is not exactly a flat bias.

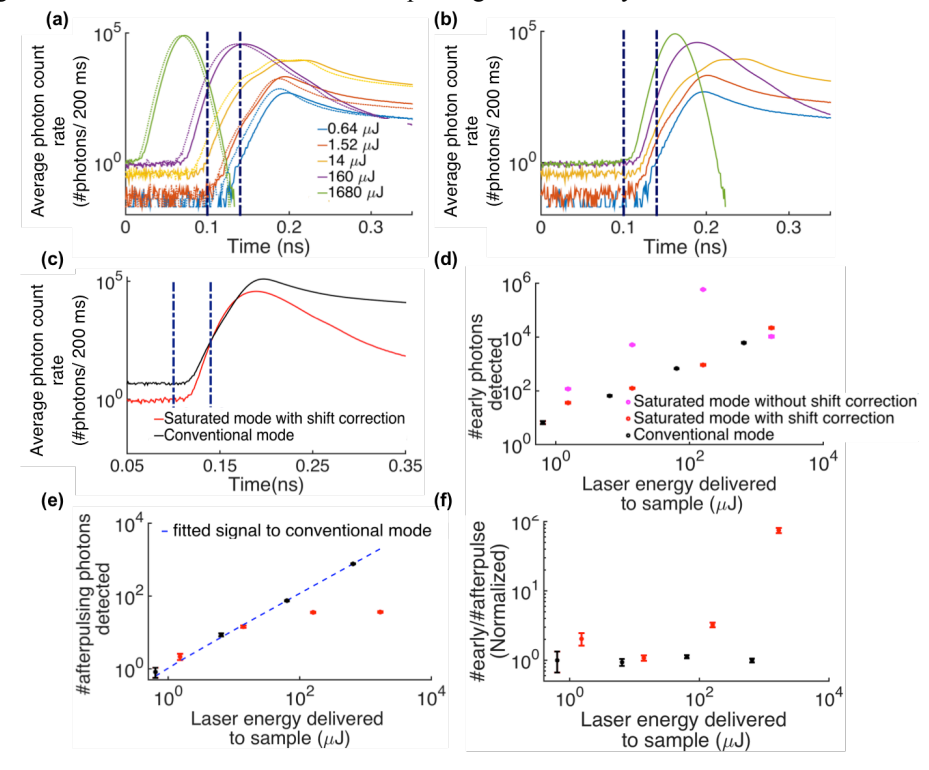


Fig 7. Linearity of early photon detection rate and increase in signal-to-background ratio (SBR) using dead-time enhanced early photon detection. (a) Temporal shift observed in both temporal point spread functions (TPSFs) - bold curves, as energy is delivered to a 2-mm-thick tissue-mimicking optical phantom ($\mu_a = 0.05 \text{ mm}^{-1}$, μ_s ' = 5 mm⁻¹) and the corresponding instrument response functions (IRF) - dotted curves, as power increases. The TPSFs are collected with saturated detector at higher incident energy. The dark blue dashed lines illustrate the range where early photons were collected.; (b) Time-shift corrected TPSFs; (c) Example TPSFs for conventional and shift-corrected saturated mode. Both curves correspond to $1.6x10^{-4}$ J energy delivered to phantom. The black data corresponds to non-saturating power of 0.01mW over 20 s of acquisition and the red data corresponds to deadtime inducing power of 1mW over 0.2 s of acquisition.; (d) Number of early photon counts detected (mean ± 2*standard deviation) as a function of light energy delivered to the sample before and after shift correction is performed.; (e) The number of background (or afterpulsed) photons detected within an equivalent range to the early photon window for the same dataset presented in (d). A linear fit is provided to the conventional mode data (blue dashed line).; (f) SBR, given by number of early to number of background photons normalized to the lowest power/shortest acquisition time for the dataset presented in (d) and (e). (b-f) Black data (SBR~1) corresponds to non-saturating laser power (~10 μW) for a range of exposure times (0.2 – 200 s) to

modify energy delivered and red data corresponds to deadtime inducing laser powers ($\sim 10~\mu W - 10~mW$) for an exposure time of 0.2 s.

The number of afterpulsing events is proportional to the total count rate. Therefore, in the conventional mode experiments described in **Section IIIB**, the number of afterpulsing events increased linearly with the laser energy delivered to the sample (**Fig. 7e**). However, in the saturated mode experiments, the number of detected afterpulsing events saturated at higher laser energies (**Fig. 7e**). This saturation was expected, matching the saturation of the total number of detected events, since, at the highest laser powers²⁰, photon incidence rates far exceeded maximum detector counting rates (1.3x10⁷ photons/s). Furthermore, the fact that the background signal saturated with counting rates saturation, is a further validation that this background is dominated by the folded afterpulsing.

Since the number of early photons remains linear with laser energy incident on the sample in the saturated mode, while the background (afterpulsing) is proportional to total number of detected photons which cannot exceed 1.3×10^7 photons/s, the saturated mode offers significant enhancements in terms of signal-to-background ratio of the early photons (**Fig. 7f**). At the highest laser power in this system, the improvement in early photon to background signal ratio was 74 ± 3 times greater in the saturated mode compared to the conventional mode for matched laser energies. This is independent of the significant improvements in acquisition time achievable by the saturated mode detection. The acquisition time of the conventional mode experiment needed to be 1000 times longer than the saturated mode experiment to detect the same number of early photons.

D. Stability of system.

To evaluate the "warm-up" time of the system, the system was turned off for 24 h. It was then turned on and the IRF was monitored in 1 s acquisitions every 5 s for 150 min at a count rate below the 5% laser repetition rate (conventional mode). Mean photon arrival time, full widths at half maximum (FWHM), and maximum intensity of the IRF are plotted over time in **Fig. 8a-c**, respectively. All parameters reached a stable threshold by 25 min with mean values of 2.1 ns, 0.04 ns and $1.1e4 \pm 328$. The drift in the IRF at early time points was found to arise from the detection system and not the laser. This was observed by keeping the detection system on, while turning off the laser in 2 different ways, either by switching off power to the driver, or through the turn key operation. After 12 hours the laser was turned back on by reversing whatever procedure was used to turn it off, and the IRF was measured as before. No appreciable drift in the IRF was observed, even at the earliest time points, and the stability of the IRF matched that observed in the first stability experiment (mean 2.11 ns, 0.04 ns and $9.98e4 \pm 276$). To summarize, it was observed that the laser does not take much time to stabilize while the TCSPC is safe to use after 25 minutes of start-up only.

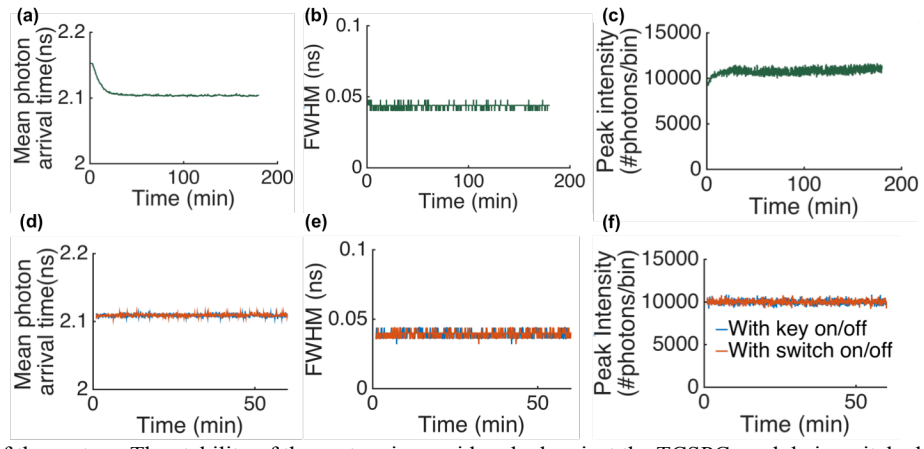


Fig 8. Stability of the system. The stability of the system is considered when just the TCSPC module is switched on alone (a-c) and also when the laser was switched on keeping the detection module on (d-f). Mean arrival time (a, d), FWHM (b, e) and peak intensity of the beam (c, f) is measured for the first few minutes after the system is switched on till the system gets to a stable state. The laser driver has both a switch and a key, while the switch turns the entire laser driver up, the key is used to turn the laser beam on. The experiment was performed at 4 ps temporal binning resolution.

E. Phantom experiment

A phantom with tissue-mimicking optical properties was made with a defined absorption pattern to test spatial resolution improvements with the presented enhanced early photon imaging system. The phantom was composed of

a USAF pattern that was printed on transparent projection paper and the paper was sandwiched between two 2-mm thick sheets (5 cm diameter circular sheets cast in a plastic petri dish) of light scattering medium in a molding process. The base material for the scattering medium was a clear polyester casting resin (Castin CraftTM, Environmental Technology Inc, Fields Landing, CA) that was mixed with titanium dioxide (DuPontTM Ti-Pure®, DuPont Titanium Technologies, Wilmington, DE) as a scatterer. 6 mg of TiO₂ were added per 1 mL of resin to achieve a reduced scattering coefficient of 5 mm⁻¹, and 10 μL of ethanol 1 per mL of resin were added to distribute the particles per layer. Next, 5 drops of catalyst (Castin CraftTM, Environmental Technology Inc, Fields Landing, CA) were added and the mixture was stirred for 1 min before being poured into the petri dish. The 2-mm thick layer was cured for an hour before placing the absorptive USAF pattern and adding the next layer. Once the final layer, which was also 2-mm thick, was added, the phantom was kept at room temperature for at least 24 h, to fully cure, before being imaged.

The phantom was imaged in two ways: with the optical projection imaging system by raster scanning TPSFs (at 1 ps histogram binning by the TCSPC) at 50- μ m intervals over a field of view of 1.5 cm x 1.5 cm (1) at a laser power of 6 μ W (conventional mode for all projections) and for 100 ms acquisitions per pixel, and (2) at a laser power of at 6 mW (saturated mode) and for a 0.1 ms acquisition at each pixel. The saturated case, with 3 orders-of-magnitude higher laser power and 3 orders-of-magnitude shorter acquisition was selected to match the early photon count rates of the conventional case. Three images were then constructed for comparison. (1) A conventional optical projection image (**Fig. 9a**), which was created by mapping the sum of the TPSFs at each projection. (2) A conventional early photon image (**Fig. 9b**), created by summing a 50-ps early time window of all conventional data TPSFs (as identified by the first 50 1-ps bins after the first non-background time-bin of the instrument response function). (3) A saturated early photon image (**Fig. 9c**), created by summing TPSFs of the high power, short acquisition time data over the same time window as in the conventional early photon image case. Contrast and contrast-to-noise ratio (CNR), as defined by Eq. (6), in the regions defined in **Fig. 9** (proximal to the 600- μ m spaced vertical bars) were calculated for each case. To quantitatively evaluate images we used contrast and contrast-to-noise ratio (CNR), defined as:

$$contrast = \frac{S_W - S_B}{S_W + S_B}, \qquad CNR = \frac{S_W - S_B}{\sqrt{\sigma_W^2 + \sigma_B^2}}, \tag{6}$$

where S_W and S_B are the maximum of the signals measured in the non-absorbing (white) and absorbing (black) region-of-interest (ROI) as defined in **Fig. 9** (proximal to 800 μ m spaced vertical bars); σ_W and σ_B are the standard deviation of the measured signals within ROI. The *contrast* values for the conventional, conventional early photon, and saturated early photon images were calculated as 0.21, 0.68, and 0.69, respectively, for an improvement of at least 3.4-fold using early photon detection over conventional mode detection. The calculated CNR values of the conventional, conventional early photon and saturated early photon images were: 3.35, 3.65, and 4.46, respectively. A small improvement in CNR of the saturated case resulted from the reduced detection rate of background afterpulsing photons in the saturated photons as demonstrated in **Fig. 7**.

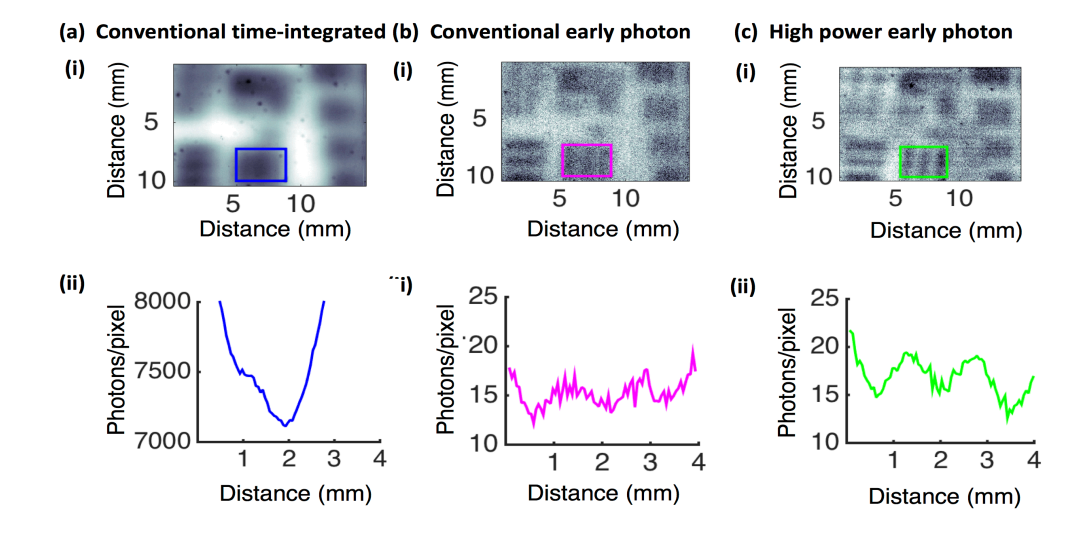


Fig 9. USAF pattern imaging. (a) Conventional optical imaging in trans-illumination mode (conventional time-integrated), which in this case is the time-integrated light intensity at every location in the image (6 µW laser power, 100 ms acquisition per position); (b) conventional early photon image (the first 50 ps of the temporal point spread functions from the data presented in (a) were integrated); and (c) saturation early photon image (high power early photon; the first 50 ps of temporal point spread function of data collected at 6 mW laser power, 0.1 ms acquisition per position were integrated). (i) Demonstrates the images of these data binning patterns and (ii) displays vertical mean intensity values obtained from the rectangular marked regions in (i).

III. CONCLUSION

This paper discusses the challenges during the construction and testing of an enhanced early photon projection system. A 3.4-fold improvement in spatial resolution was demonstrated by employing early photon detection over conventional optical projection imaging. Moreover, with a relatively modest power femtosecond pulsed laser (12 mW), early photon detection rates were 3 orders of magnitude greater than that achievable for detection in conventional mode (reducing needed acquisition time 1000-fold), and signal-to-background improvements of over 70-times were observed. Future work will further advance enhanced early photon detection by including the addition of angular domain constriction on detected photon (for further restriction of late photon detection)¹⁴, adding a more powerful laser, and adapting the system to 3D tomography applications in fluorescence and tissue samples.

IV. ACKNOWLEDGMENTS

The authors acknowledge support from the NSF CAREER 1653627, the Nayar Prize at IIT, the Pritzker Institute of Biomedical Science and Engineering, the Medical Imaging Research Center (MIRC) and the Department of Biomedical Engineering at the Illinois Institute of Technology.

V. REFERENCES

- ¹D. H. Brewster, J. Crichton, J. C. Harvey, G. Dawson and E. R. Nairn Journal of clinical pathology **49**, (1996).
- ²R. Weissleder and M. J. Pittet Nature **452**, (2008).
- ³D. L. Longo The New England journal of medicine **366**, (2012).
- ⁴I. Stoffels, S. Morscher, I. Helfrich, U. Hillen, J. Leyh, N. C. Burton, T. C. Sardella, J. Claussen, T. D. Poeppel, H. S. Bachmann, A. Roesch, K. Griewank, D. Schadendorf, M. Gunzer and J. Klode Science translational medicine 7, (2015).
- ⁵K. M. Tichauer, K. S. Samkoe, J. R. Gunn, S. C. Kanick, P. J. Hoopes, R. J. Barth, P. A. Kaufman, T. Hasan and B. W. Pogue Nature medicine 20, (2014).
- ⁶V. Ntziachristos Nature methods 7, (2010).
- ⁷S. L. Jacques Physics in medicine and biology **58**, (2013).
- ⁸J. Sharpe, U. Ahlgren, P. Perry, B. Hill, A. Ross, J. Hecksher-Sorensen, R. Baldock and D. Davidson Science 296, (2002). ⁹V. V. Tuchin J Phys D Appl Phys **38,** (2005).
- ¹⁰L. Wang, P. P. Ho, C. Liu, G. Zhang and R. R. Alfano Science **253**, (1991).
- ¹¹M. J. Niedre, R. H. de Kleine, E. Aikawa, D. G. Kirsch, R. Weissleder and V. Ntziachristos Proceedings of the National Academy of Sciences of the United States of America 105, (2008).
- ¹²A. Bassi, D. Brida, C. D'Andrea, G. Valentini, R. Cubeddu, S. De Silvestri and G. Cerullo Optics letters 35,
- ¹³W. Tan, Z. Zhou, A. Lin, J. Si, P. Zhan, B. Wu and X. Hou Optics express 21, (2013).
- ¹⁴F. Vasefi, B. Kaminska, G. H. Chapman and J. J. Carson Optics express **16**, (2008).
- ¹⁵Y. Pu and D. Psaltis Applied optics **52**, (2013).
- ¹⁶F. O. Fahrbach, P. Simon and A. Rohrbach Nat Photonics **4**, (2010).
- ¹⁷V. Y. Soloviev and S. R. Arridge Biomedical optics express **2**, (2011).
- ¹⁸F. Yang, M. S. Ozturk, L. Zhao, W. Cong, G. Wang and X. Intes IEEE transactions on bio-medical engineering 62,
- ¹⁹K. Tanaka, Y. Mukaigawa, H. Kubo, Y. Matsushita and Y. Yagi, *Proceedings of Proceedings of the IEEE* Conference on Computer Vision and Pattern Recognition.
- ²⁰L. Sinha, J. G. Brankov and K. M. Tichauer Optics letters **41**, (2016).
- ²¹K. Tichauer, R. W. Holt, F. Leblond and B. W. Pogue, *Proceedings of Proceedings of SPIE*.

- ²²L. Fieramonti, A. Bassi, E. A. Foglia, A. Pistocchi, C. D'Andrea, G. Valentini, R. Cubeddu, S. De Silvestri, G. Cerullo and F. Cotelli PloS one **7**, (2012). ²³Y. Mu and M. Niedre Conf Proc IEEE Eng Med Biol Soc **2014**, (2014).
- ²⁴M. Niedre and V. Ntziachristos Optics letters **35**, (2010).
- ²⁵G. M. Turner, G. Zacharakis, A. Soubret, J. Ripoll and V. Ntziachristos Optics letters **30**, (2005).
- ²⁶J. Wu, L. Perelman, R. R. Dasari and M. S. Feld Proceedings of the National Academy of Sciences of the United States of America **94**, (1997).
- ²⁷F. Leblond, H. Dehghani, D. Kepshire and B. W. Pogue Journal of the Optical Society of America. A, Optics, image science, and vision 26, (2009).
- ²⁸Y. Mu and M. Niedre Biomedical optics express **6**, (2015).
- ²⁹Y. Mu, N. Valim and M. Niedre Optics letters **38**, (2013).
- ³⁰W. Becker, Advanced time-correlated single photon counting (Springer, 2005).
- ³¹G. Kirchner and F. Koidl J Opt a-Pure Appl Op **1**, (1999).
- ³²D. A. Gedcke, edited by O. A. N. AN57 (2001).
- ³³M. S. Patterson, B. Chance and B. C. Wilson Applied optics **28**, (1989).
- ³⁴H. Kogelnik and T. Li Applied optics **5**, (1966).
- ³⁵K. Konig Journal of microscopy **200**, (2000).
- ³⁶S. Donati and T. Tambosso Ieee J Sel Top Quant **20**, (2014).
- ³⁷A. C. Giudice, M. Ghioni, S. Cova and F. Zappa, *Proceedings of Proc. Eur. Solid-State Device Res. Conf.*